Front. Mater. Sci. 2025, 19(2): 250718
https://doi.org/10.1007/s11706-025-0718-z

RESEARCH ARTICLE

Surface engineering on Co_3O_4 through quenching with cold salt solution for enhance oxygen evolution reaction

Chaoxiang Li[1*], Chao Huang[1*], Xiaodan Chi[2], Pei Zhou[1], Changchang Wang[1], Wenhui Yao[1], Ziyao Zhou[1], and Liqian Wu (✉)[1]

1 Micro-Electronics Research Institute, Hangzhou Dianzi University, Hangzhou 310018, China
2 Department of Basic, Dalian Naval Academy, Dalian 116018, China

ABSTRACT: The surface engineering has been testified to be an effective strategy for optimizing oxygen evolution reaction (OER) activity. Nevertheless, many of these techniques involve complex and multiple synthesis process, which leads to potential safety hazards, raises the cost of production, and hinders the scaled-up application. Herein, a facile strategy (i.e., quenching with lanthanum nitrate cold salt solution) was adopted to fabricate the surface of Co_3O_4 grown on nickel foam, and boost the electrocatalytic performance for OER. Analyses of the experimental results show that the surface engineering strategy can induce many defects on the surface of Co_3O_4, including microcracks and oxygen vacancies, which provides more active sites for electrochemical reaction. Consequently, the treated sample exhibits significantly improved OER electrocatalytic activity, requiring only 311 mV to deliver 100 mA·cm^{-2} for OER in alkaline solution. This work highlights the feasibility of designing advanced electrocatalysts towards OER via quenching and extends the use of quenching chemistry in catalysis.

KEYWORDS: electrocatalysis; oxygen evolution reaction; spinel oxide; surface engineering; cold salt solution quenching

Contents

Received August 20, 2024; accepted January 9, 2025

E-mail: wulq@hdu.edu.cn

∗ C.L. and C.H. contributed equally to this work.

1 Introduction

Recently, the increasingly urgent energy and

environmental crises originating from the excessive exploitation of fossil fuels have driven people to explore new alternative energy resources. Thereinto, hydrogen energy is recognized as an ideal fuel alternative in the future because of its high energy density and zero carbon emission [1–3]. Among various techniques suggested for hydrogen generation, water splitting, facilitated by sustainable and eco-friendly power sources including wind and solar power, stands out as one of the cleanest and most convenient approaches [4–6]. The water electrolysis process consists of a cathodic hydrogen evolution reaction (HER) [7] and an anodic oxygen evolution reaction (OER) [8]. Since OER involves multiple proton coupling and electron transfer processes, the reaction kinetics are impeded, and the water decomposition efficiency is lowered [9–10]. It is indispensable to introduce electrocatalysts towards OER to expedite the reaction kinetics during water electrolysis. Currently, OER electrocatalysts derived from noble metal-based oxides (e.g., RuO_2 and IrO_2) are recognized for their superior efficacy, but their limited availability and high economic costs pose significant challenges to their broader implementation in the industrial domain [11–13]. Consequently, considerable resources have been invested in the research and development of non-precious catalysts.

Spinel-structured oxides of AB_2O_4 (A, B = metal), where A^{2+} ions are typically positioned within the tetrahedron sites (A_{Td}) and B^{3+} ions are housed in the octahedron sites (B_{Oh}), have been increasingly recognized as cost-effective electrocatalysts due to their earth-abundant characteristics, anticorrosion stability, and rich redox properties [14–15]. Particularly, as a prototypical spinel oxide electrocatalyst, Co_3O_4 has garnered significant attention for its excellent OER electrocatalytic activity and electrochemical stability in alkaline media [16–17]. Unfortunately, the scarcity of active sites and the intrinsically low electrical conductivity greatly restrict the electrocatalytic behavior for Co_3O_4 during the OER process, resulting in unsatisfactory activity. To address these issues, many strategies have been tried out and adopted by scholars [18–22].

Surface engineering has been considered an effective strategy. By regulating the surface morphology and composition of electrocatalysts, the electrochemical performance is optimized. To date, several surface engineering techniques have been reported, including plasma treatment, electrochemical deposition (ECD), atomic layer deposition (ALD), nitridation/sulfidation/phosphorization treatment, and alkali-etching treatment [23–25]. However, many of these techniques involve complex and multiple synthesis processes, or potential safety hazards, which increase the cost of production and obstruct the scale-up application [26]. Quenching, originally applied to the steel manufacturing process, involves calcining the material at a specific temperature and cooling it rapidly in quenching medium [27–28]. The temperature plunge preserves lots of ion disorders and vacancies from high temperature to room temperature, producing many microcracks caused by unevenly thermal stress, which increases the number of electrocatalytic active sites. Therefore, quenching is an effective strategy for introducing surface defects on electrocatalysts. Additionally, since the element with distinct atomic radius difference is prone to incur distortions when doped into lattice, doping with rare-earth elements (REEs) is also expected to easily generate defects on the surface of Co_3O_4.

Herein, we treated the surface of Co_3O_4 grown on nickel foam (NF) through quenching with lanthanum nitrate cold salt solution. The treated sample evidently exhibited promoted OER electrocatalytic activity and good stability, requiring only 311 mV to deliver 100 $mA \cdot cm^{-2}$ for OER in alkaline solution. On the basis of experimental analysis, the origin of the enhanced OER activity is further expounded.

2 Experimental

2.1 Materials

All chemical reagents in this study were used as received without further purification. NF was purchased from Jiangsu Kunshan Jiayisheng Electronics Co., Ltd., cobalt nitrate ($Co(NO_3)_2 \cdot 6H_2O$), ammonium fluoride (NH_4F), urea (CH_4N_2O), and lanthanum nitrate ($La(NO_3)_3 \cdot 6H_2O$) were from Shanghai Macklin Biochemical Co., Ltd., while anhydrous ethanol was from Hangzhou Shuanglin Chemical Reagent Co., Ltd. High-purity deionized water (DIW) used in this work was obtained through a laboratory-grade water purification apparatus manufactured by Shanghai Hetai Co., Ltd.

2.2 Synthesis of electrocatalysts

The process performed to prepare quenched Co_3O_4 is

illustrated in Scheme 1. NF was firstly cut into standard sizes of 1 cm × 3 cm and sonicated in dilute hydrochloric acid for 20 min to remove surface oxides. Then, NF was sonically cleaned alternatively with DIW and ethanol, each for a duration of 20 min, and kept in a vacuum oven at 60 °C for 8 h to ensure drying completely. Afterwards, $Co(NO_3)_2·6H_2O$ (1.5 mmol), NH_4F (3 mmol), and CH_4N_2O (5 mmol) were dissolved in DIW (15 mL) followed by stirring vigorously for 30 min to obtain a uniform solution which was transferred together with a clean piece of NF into a 25 mL polytetrafluoroethylene (PTFE) lining. The liner was subsequently placed in a stainless-steel autoclave and heated to 120 °C in an oven for 12 h. After reaction, the nanowire array precursor grown directly on NF was removed and washed thoroughly several times alternately with DIW and ethanol, placed into a vacuum drying oven at 60 °C for 8 h, and further heated to 350 °C at a rate of 2 °C·min^{-1} under air atmosphere for 2 h. Immediately after the calcination, one sample was put into 1 mol·L^{-1} $La(NO_3)_3·6H_2O$ solution at 0 °C for quenching experiments. For comparison, under the same experimental conditions, one set of samples prepared was naturally cooled in air, while another set of samples prepared was cooled in ice water at 0 °C. To facilitate the description, hereafter the air-cooled sample will be referred to as Co_3O_4, the ice water-quenched sample as Co_3O_4-Q, and the cold salt solution-quenched sample as Co_3O_4-Q-La.

2.3 Material characterizations

X-ray diffraction (XRD) patterns were obtained using a Rigaku D/max 2500 instrument equipped with the Cu Kα (λ = 1.5418 Å) radiation source. Field emission scanning electron microscopy (FESEM) images were obtained using a Zeiss Sigma 300 microscope (Germany). Transmission electron microscopy (TEM) images were obtained using a JEOL-2010F system. Composition mappings were ascertained through energy dispersive X-ray spectroscopy (EDX) conducted on the TEM instrument. The chemical composition at the sample surface was characterized through X-ray photoelectron spectroscopy (XPS) using an EscaLab 250Xi XPS spectrometer (Thermo Fisher Scientific, USA), and the XPS spectrum was calibrated with standard C 1s peaks to determine precise energy level positions. Electron paramagnetic resonance (EPR) spectra were measured using a Bruker EMX-Plus instrument (Bruker, Germany).

2.4 Electrochemical measurements

Electrochemical tests were conducted at room temperature using a typical three-electrode configuration on the CHI760D electrochemical workstation. An Ag/AgCl electrode with saturated KCl solution served as the reference electrode while a graphite rod functioned as the counter electrode. The prepared electrocatalysts on NF were cut into size 1 cm × 1 cm, directly used as the working electrode for electrochemical measurements. Tests were carried out in 1 mol·L^{-1} KOH electrolyte, and all potentials are converted to the reversible hydrogen electrode (RHE) scale according to Eq. (1) as follows:

$$E_{RHE}=E_{Ag/AgCl}+0.059\times pH+E^{\circ}_{Ag/AgCl} \quad (pH = 14) \quad (1)$$

where $E_{Ag/AgCl}$ is the experimentally measured potential *vs.* Ag/AgCl and $E^{\circ}_{Ag/AgCl}$ is 0.197 V at 25 °C. The potential values provided along the text are referenced against RHE unless otherwise stated.

Before linear sweep voltammetry (LSV) and cyclic

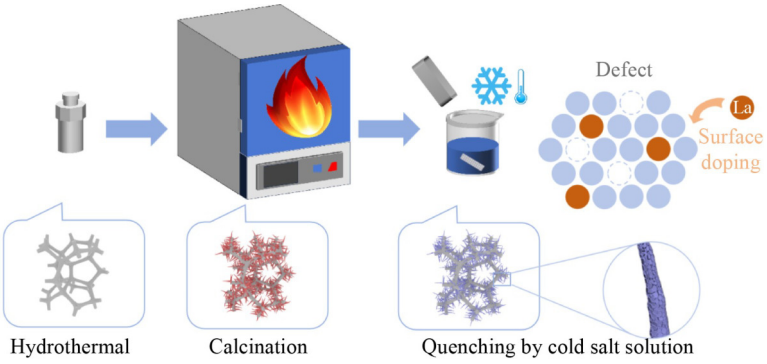

Scheme 1 Schematic illustration for the preparation process of Co_3O_4-Q-La.

voltammetry (CV) measurements on samples, the performance stability of the working electrode was ensured through a CV test at a scan rate of 100 $mV \cdot s^{-1}$. The LSV curves were measured at a scan rate of 5 $mV \cdot s^{-1}$, and the *IR* compensation was performed to correct the potential drop caused by the solution Ohm resistance. The Tafel slope is calculated using the LSV curve recorded above, according to the Tafel equation which is as follows:

$$\eta = a + b \log |J| \tag{2}$$

where η is the overpotential, a is the cathode intercept related to the exchange current density, b is the slope, and J is the current density. The double-layer capacitance (C_{dl}) was deduced from the analysis of the CV curve. The measured potential range is from 0.83 to 1.03 V (*vs.* RHE), and the scan rate is from 20 to 60 $mV \cdot s^{-1}$. Electrochemical impedance spectroscopy (EIS) was further carried out in the frequency range from 0.01 Hz to 100 kHz at a potential of 1.53 V (*vs.* RHE) with the amplitude of 5 mV. The stability of the electrode was evaluated through long-term CV cycling, which was performed for 1000 cycles, and chronopotentiometry, which was conducted at a current density of 60 $mA \cdot cm^{-2}$ for over 35 h.

3 Results and discussion

3.1 Microstructural characterizations

FESEM and TEM were first carried out to observe and discuss the impact of quenching on morphologies of Co_3O_4 series samples. Figures 1(a) and 1(b) depict SEM images of Co_3O_4 cooled in air, where the uniformly arranged nano-needle structure coat the surface of NF. In comparison, the images of Co_3O_4-Q quenched in ice water (Fig. S1 (included by ESM of Appendix)) and Co_3O_4-Q-La (Figs. 1(c) and 1(d)) quenched in cold solution show different clustered array structures. This is caused by the cold shrinkage of samples during rapid cooling, which enables the nano-needle structure to be retained after quenching. Further, more detailed microstructure information was obtained through TEM. Identical to the morphology results observed via SEM, the TEM image (Fig. 1(e)) of Co_3O_4 cooled in air demonstrates a relatively smooth and flat surface for the needle structure. However, the quenched surface of Co_3O_4-Q-La presents a jagged structure consisting of many nanoparticles (Fig. 1(f)), which may result from the microcrack effect induced by the uneven thermal stress during quenching. The porous nanowire structure would facilitate the exposure of more active sites and the faster charge exchange between the electrode and the electrolyte, leading to improved electrochemical performance [29].

The crystal structures of Co_3O_4 series samples were characterized and studied through XRD, as depicted in Fig. 1(g). Three distinct diffraction peaks at nearly 44.5°, 51.8°, and 76.4° are attributable to crystallographic planes of (1 1 1), (2 0 0), and (2 2 0) within the Ni metal (JCPDS No. 04-0850), respectively, whereas other visible diffraction peaks are assigned to cubic Co_3O_4 (JCPDS No. 42-1467). Except for those observed in NF and Co_3O_4, no additional diffraction peaks were detected in Co_3O_4 series samples, ruling out the possibility of the generation of the discrete secondary phase during quenching. To further study the crystal structure of the treated sample, the high-resolution TEM (HRTEM) image for Co_3O_4-Q-La is supplied in Fig. 1(h). The observed interplanar spacing of 0.24 nm corresponds to the (3 1 1) plane lattice of Co_3O_4, matching well with the XRD result. Furthermore, the elemental mappings (Fig. 1(i)) of La, Co, and O suggest that the La element is successfully doped onto the surface of Co_3O_4 through quenching with the lanthanum nitrate cold salt solution [30].

3.2 Electrocatalytic performance

To gain insights into the effects of quenching with lanthanum nitrate cold salt solution on OER activities, the OER electrocatalytic performance of Co_3O_4 series samples was measured in 1 $mol \cdot L^{-1}$ KOH solution. Figure 2(a) depicts OER polarization curves, with corresponding overpotential values listed in Table 1. It is revealed that the Co_3O_4-Q-La sample exhibits a low overpotential of 311 mV at 100 $mA \cdot cm^{-2}$, significantly smaller than those of Co_3O_4-Q (337 mV) and Co_3O_4 (348 mV). In the corresponding Tafel plots (Fig. 2(b)), the Tafel slope for Co_3O_4-Q-La is 75 $mV \cdot dec^{-1}$, apparently lower than those observed for both Co_3O_4-Q (137 $mV \cdot dec^{-1}$) and Co_3O_4 (153 $mV \cdot dec^{-1}$). Such results indicate that the surface treatment through quenching with lanthanum nitrate cold salt solution can effectively strengthen the OER reaction kinetics and enhance the OER electrocatalytic performance. As illustrated in Fig. 2(c), the double-layer capacitance (C_{dl}) plots of series

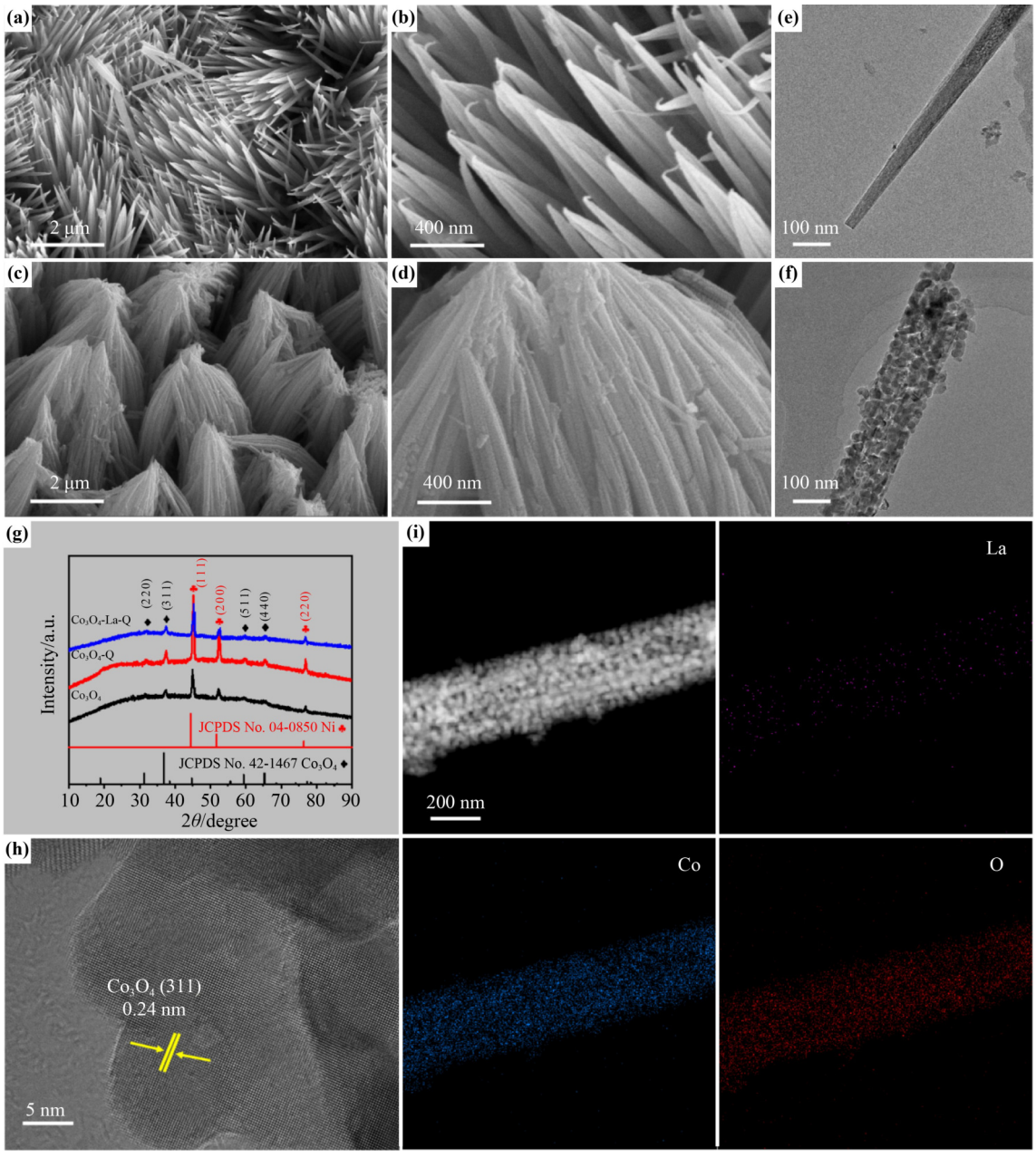

Fig. 1 (**a**)(**b**) FESEM images of Co_3O_4 at low and high magnifications. (**c**)(**d**) FESEM images of Co_3O_4-Q-La at low and high magnifications. (**e**)(**f**) TEM images of Co_3O_4 (upper) and Co_3O_4-Q-La (lower). (**g**) XRD patterns of a series of Co_3O_4 samples. (**h**) HRTEM image and (**i**) EDX mapping images of Co_3O_4-Q-La.

samples are depicted, derived from CV curves shown in Fig. S2 (included by ESM of Appendix) in a non-faradic potential region under OER measurements. The obtained C_{dl} values for Co_3O_4, Co_3O_4-Q, and Co_3O_4-Q-La are 79.1, 82.2, and 127.4 $mF \cdot cm^{-2}$, respectively. Obviously, Co_3O_4-Q-La possesses the largest electrochemcial surface area (ECSA) and the most OER active sites, consistent with its optimal OER electrocatalytic performance. To distinguish the charge transport ability during the OER process, EIS was conducted. Based on data presented in Fig. 2(d) and Table 1, the R_{ct} value of Co_3O_4-Q-La is obtained to be 2.93 Ω, which is significantly smaller than those of Co_3O_4-Q (5.75 Ω) and Co_3O_4 (9.04 Ω), indicating that Co_3O_4-Q-La exhibits the highest charge transfer efficiency (CTE) among Co_3O_4 series samples.

For the assessment of stability towards OER, long-term CV cycling and chronopotentiometry tests were executed. Figure 2(e) illustrates that the polarization curve of

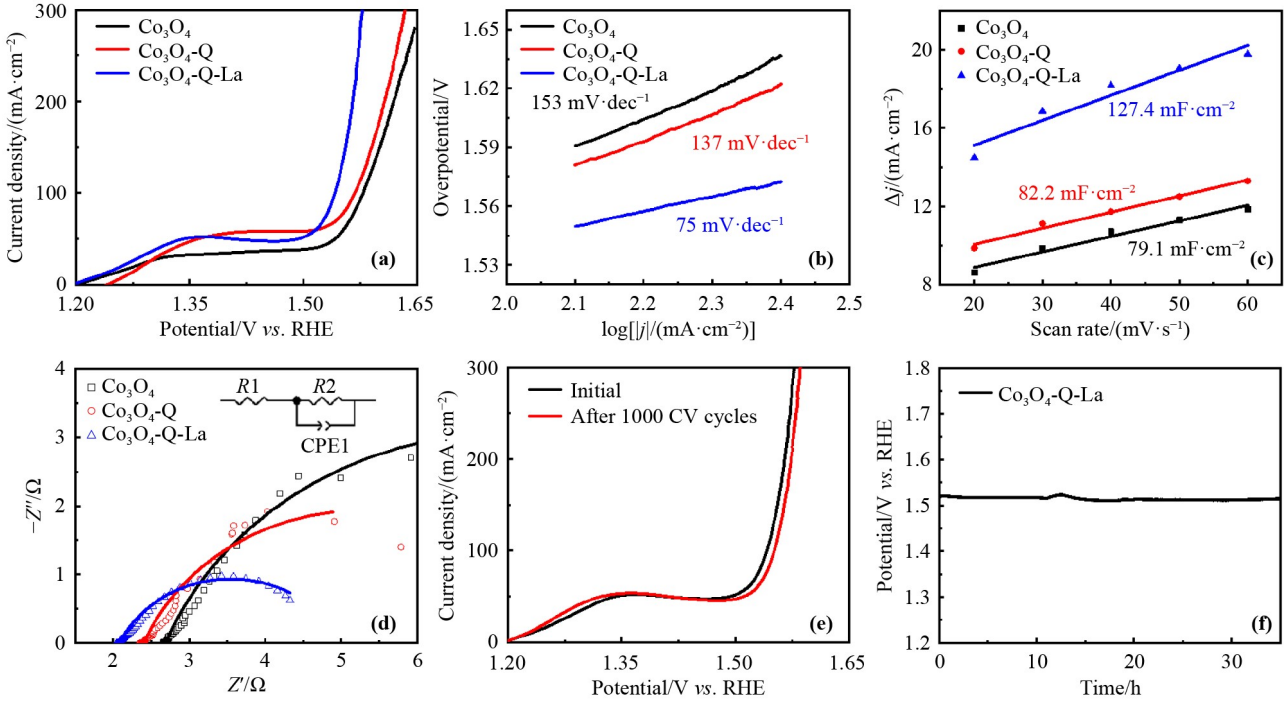

Fig. 2 (**a**) OER polarization curves, (**b**) corresponding Tafel plots, (**c**) Nyquist plots, and (**d**) double-layer capacitance (C_{dl}) plots of Co_3O_4 series samples. (**e**) Cyclic stability test result and (**f**) chronopotentiometry curve of Co_3O_4-Q-La.

Table 1 Electrochemical oxygen evolution parameters for Co_3O_4 series samples

Sample	η_{100}/mV	Tafel slope/(mV·dec^{-1})	C_{dl}/(mF·cm^{-2})	R_{ct}/Ω
Co_3O_4	348	153	79.1	9.04
Co_3O_4-Q	337	137	82.2	5.75
Co_3O_4-Q-La	311	75	127.4	2.93

Note: η_{100} refers to the overpotential at 100 mA·cm^{-2}.

Table 2 Comparison of the Co_3O_4-Q-La electrocatalyst with other oxygen evolution electrocatalysts

Sample	η_{100}/mV	Tafel slope/(mV·dec^{-1})	Ref.
Co_3O_4-Q-La	311	75	This work
Co_2P-Co_3O_4/C	322	69.5	[31]
H-Fe_3O_4@FeP@NC	310	41.3	[32]
$CuMoO_4$@Co_3O_4	376	87.4	[33]
$Mn_{1.2}Co_{1.8}O_4$	292	76.3	[34]
NCO@RuO_2-NCs	283	74.3	[35]

Co_3O_4-Q-La after 1000 CV cycles closely resembles its initial state. The chronopotentiometry test (Fig. 2(f)) reveals minimal fluctuation or decay of overpotential at 60 mA·cm^{-2} after continuous testing for 35 h. Both the long-term CV cycling and the chronoamperometry tests verify the long-term stability towards OER. Additionally, the boosted OER electrocatalytic performance is also comparable to those of other spinel-based OER electrocatalysts, including CoP-Co_3O_4/C [31], H-Fe_3O_4@FeP@NC [32], $CuMoO_4$@Co_3O_4 [33], $Mn_{1.2}Co_{1.8}O_4$ [34], and NCO@RuO_2-NCs [35] (see details in Table 2).

3.3 Probing the origin of enhanced OER performance

Why does the treated sample in this work exhibit improved OER electrocatalytic activity? Firstly, the XPS analysis was implemented to understand the influence of quenching on the surface chemical states of Co_3O_4 series samples. Figure 3(a) displays the La 3d high-resolution XPS spectrum, where two peaks located at 835.3 and 838.7 eV are assigned to La $3d_{5/2}$ of La^{3+} and the corresponding satellite peak, respectively [36–37]. This testifies that the La element is doped on the surface of the sample, in agreement with the EDX-mapping results mentioned above. Figure 3(b) depicts Co 2p high-resolution XPS spectra of Co_3O_4 series samples. The deconvolution of Co 2p spectra reveals that the Co $2p_{3/2}$ spectrum in Co_3O_4 contains two component peaks (Co^{3+} and Co^{2+}) and two shake-up satellite peaks (Sat. 1 and Sat. 2), where the peaks at 779.6 and 780.8 eV are specifically assigned to Co^{3+} and Co^{2+}, respectively,

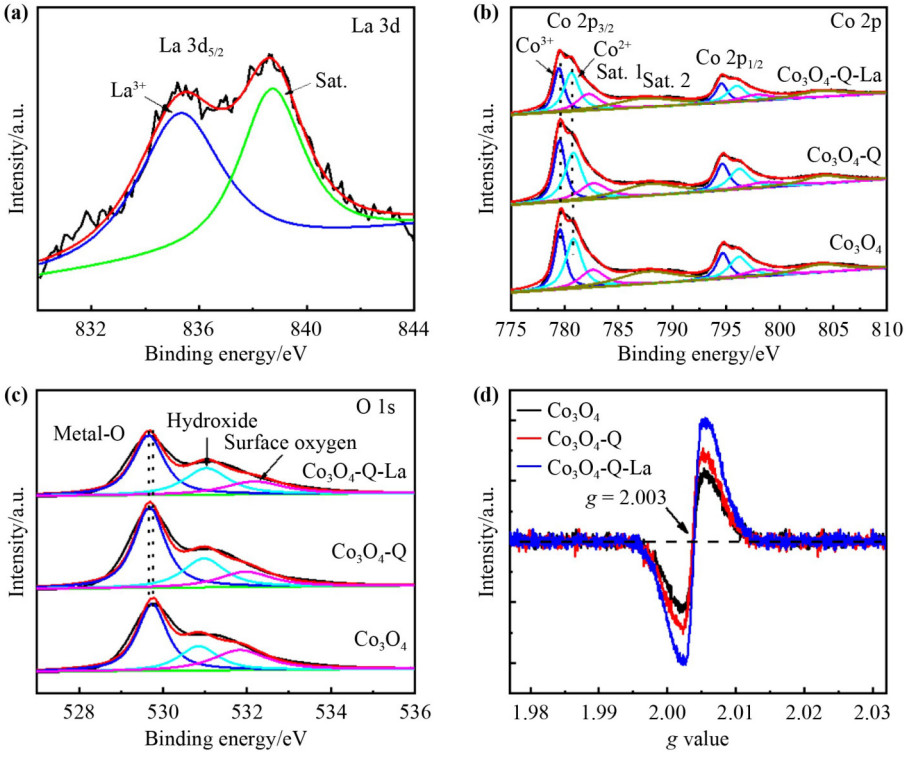

Fig. 3 (**a**) High-resolution XPS spectrum of La 3d for Co_3O_4-Q-La. (**b**)(**c**) High-resolution XPS spectra of Co 2p and O 1s for Co_3O_4 series samples. (**d**) EPR spectra for Co_3O_4 series samples.

while the other peaks located at 782.6 and 787.9 eV are associated with their satellite peaks [38]. Compared to Co_3O_4, it is observed that there is no obvious shift between Co 2p peaks for other two samples, indicating that the La element doping has little influence on the electronegativity of the Co species [36]. As illustrated in Fig. 3(c), the O 1s XPS spectrum of Co_3O_4 is characterized by three peaks, with one peak of 529.8 eV attributed to the metal-oxygen bonding (Co−O bonding), another peak of 531 eV assigned to the surface hydroxides, and a third peak of 531.8 eV attributable to the surface adsorbed oxygen functional groups [39]. A comparison of the O 1s spectra of the samples with those of Co_3O_4 reveals an obvious shift of the peaks associated with the Co−O bond to lower binding energies, suggesting the increased amount of defects such as oxygen vacancies onto the sample surface.

As a useful technique for detecting oxygen vacancies and disordered regions, EPR enables a more detailed evaluation on the effect of quenching on the surface of Co_3O_4 series samples [40]. As shown in Fig. 3(d), an obvious EPR signal at g = 2.003 is observed in all Co_3O_4 series samples, demonstrating the existence of oxygen vacancies. The higher EPR signal intensity signifies the larger concentration of oxygen vacancies. From Fig. 3(d), it can be seen that the quenched samples (Co_3O_4-Q and Co_3O_4-Q-La) display much stronger resonance signals than that of the Co_3O_4 sample, which serves to underscores the effectiveness of quenching as a strategy to increase defects including oxygen vacancies [41]. Besides, for the two quenched samples, the resonance signal of Co_3O_4-Q-La is stronger than that of Co_3O_4-Q, revealing that the introduction of the La element can further increase the concentration of oxygen vacancies on the sample surface. It is probably incurred from the large difference in atomic radii between La ions and Co ions that creates the lattice distortion. These defects can serve as active sites for the optimization of the OER electrocatalytic activity.

On the basis of above experimental analyses, the main reason for the enhancement in the OER activity can be summed up as follows: the doping of the La element promotes the generation of oxygen vacancies, serving as active sites, on the surface of Co_3O_4. Meanwhile, benefiting from the temperature plunge, the quenched surface exhibits microcracks, resulting in the exposure of

more catalytically active sites.

4 Conclusions

In conclusion, we have demonstrated that the surface treatment through quenching with lanthanum nitrate cold salt solution can effectively improve the OER activity of Co_3O_4. Experimental analyses suggest that this surface engineering strategy can induce many defects on the Co_3O_4 surface, including microcracks and oxygen vacancies, which provide more active sites for the electrochemical reaction. The treated sample evidently exhibits promoted OER electrocatalytic activity, requiring only 311 mV to deliver 100 $mA \cdot cm^{-2}$ for OER in alkaline solution. This work highlights the feasibility of designing advanced electrocatalysts towards OER via quenching and extends the use of quenching chemistry in catalysis.

Declaration of competing interest The authors declare that they have no known competing financial interests or personal relationships that could have appeared to influence the work reported in this paper.

Acknowledgements The authors acknowledge the support from the National Natural Science Foundation of China (52101215) and the Natural Science Foundation of Liaoning Province, China (2024-BS-315).

Data availability statement The data that support the findings of this study are available from the corresponding author upon reasonable request.

Online appendix Electronic supplementary material (ESM) can be found in the online version at https://doi.org/10.1007/s11706-025-0718-z and https://journal.hep.com.cn/foms/EN/10.1007/s11706-025-0718-z that includes Figs. S1–S2,

References

[1] Wang J, Cui W, Liu Q, et al. Recent progress in cobalt-based heterogeneous catalysts for electrochemical water splitting. Advanced Materials, 2016, 28(2): 215−230

[2] Yu L, Mishra I K, Xie Y L, et al. Ternary $Ni_{2(1-x)}Mo_{2x}P$ nanowire arrays toward efficient and stable hydrogen evolution electrocatalysis under large-current-density. Nano Energy, 2018, 53: 492−500

[3] Yuan K, Cao Q, Li X, et al. Synthesis of WO_3@$ZnWO_4$@ZnO–ZnO hierarchical nanocactus arrays for efficient photoelectrochemical water splitting. Nano Energy, 2017, 41: 543−551

[4] Agyekum E B, Nutakor C, Agwa A M, et al. A critical review of renewable hydrogen production methods: factors affecting their scale-up and its role in future energy generation. Membranes, 2022, 12(2): 173

[5] Pareek A, Dom R, Gupta J, et al. Insights into renewable hydrogen energy: recent advances and prospects. Materials Science for Energy Technologies, 2020, 3: 319−327

[6] Worku A K, Ayele D W, Deepak D B, et al. Recent advances and challenges of hydrogen production technologies via renewable energy sources. Advanced Energy and Sustainability Research, 2024, 5(5): 2300273

[7] Anantharaj S, Noda S, Jothi V R, et al. Strategies and perspectives to catch the missing pieces in energy-efficient hydrogen evolution reaction in alkaline media. Angewandte Chemie International Edition, 2021, 60(35): 18981−19006

[8] Chen F Y, Wu Z Y, Adler Z, et al. Stability challenges of electrocatalytic oxygen evolution reaction: from mechanistic understanding to reactor design. Joule, 2021, 5(7): 1704−1731

[9] Song J, Wei C, Huang Z F, et al. A review on fundamentals for designing oxygen evolution electrocatalysts. Chemical Society Reviews, 2020, 49(7): 2196−2214

[10] Zhang K, Zou R. Advanced transition metal-based OER electrocatalysts: current status, opportunities, and challenges. Small, 2021, 17(37): 2100129

[11] Tian L, Li Z, Xu X, et al. Advances in noble metal (Ru, Rh, and Ir) doping for boosting water splitting electrocatalysis. Journal of Materials Chemistry A: Materials for Energy and Sustainability, 2021, 9(23): 13459−13470

[12] Wang C, Shang H, Li J, et al. Ultralow Ru doping induced interface engineering in MOF derived ruthenium–cobalt oxide hollow nanobox for efficient water oxidation electrocatalysis. Chemical Engineering Journal, 2021, 420: 129805

[13] Chen G, Yin Q, Li X, et al. Engineering Co vacancy at tetrahedral site in spinel Co_3O_4 to enhance the oxygen evolution reaction performance in alkaline and neutral electrolyte. Fuel, 2024, 378: 132863

[14] Gao L K, Cui X, Wang Z W, et al. *Operando* unraveling photothermal-promoted dynamic active-sites generation in $NiFe_2O_4$ for markedly enhanced oxygen evolution. Proceedings of the National Academy of Sciences of the United States of America, 2021, 118(7): e2023421118

[15] Janani G, Chae Y, Surendran S, et al. Rational design of spinel oxide nanocomposites with tailored electrochemical oxygen evolution and reduction reactions for zinc air batteries. Applied Sciences, 2020, 10(9): 3165

[16] Yue X, Qin X, Chen Y, et al. Constructing active sites from atomic-scale geometrical engineering in spinel oxide solid solutions for efficient and robust oxygen evolution reaction electrocatalysts. Advanced Science, 2021, 8(17): 2101653

[17] Wiegmann T, Pacheco I, Reikowski F, et al. *Operando* identification of the reversible skin layer on Co_3O_4 as a three-

dimensional reaction zone for oxygen evolution. ACS Catalysis, 2022, 12(6): 3256−3268

[18] An L, Zhang H, Zhu J M, et al. Balancing activity and stability in spinel cobalt oxides through geometrical sites occupation towards efficient electrocatalytic oxygen evolution. Angewandte Chemie International Edition, 2023, 62(3): e202214600

[19] Wu J, Wang X, Zheng W, et al. Identifying and interpreting geometric configuration-dependent activity of spinel catalysts for water reduction. Journal of the American Chemical Society, 2022, 144(41): 19163−19172

[20] Liu T, Yang S, Guan J, et al. Quenching as a route to defect-rich Ru-pyrochlore electrocatalysts toward the oxygen evolution reaction. Small Methods, 2022, 6(1): 2101156

[21] Zhou Y, Sun S, Wei C, et al. Significance of engineering the octahedral units to promote the oxygen evolution reaction of spinel oxides. Advanced Materials, 2019, 31(41): 1902509

[22] Zhang W, Chen G, Du Y, et al. Large-scale synthesis of Fe-doped amorphous cobalt oxide electrocatalysts at room temperature for the oxygen evolution reaction. ACS Applied Energy Materials, 2022, 5(3): 3129−3136

[23] Wang Y, Meng C, Zhao L, et al. Surface and near-surface engineering design of transition metal catalysts for promoting water splitting. Chemical Communications, 2023, 59(56): 8644−8659

[24] Kong F, Shi W, Song Y, et al. Surface/near-surface structure of highly active and durable Pt-based catalysts for oxygen reduction reaction: a review. Advanced Energy and Sustainability Research, 2021, 2(7): 2100025

[25] Zhang W, Li X, Chen G, et al. Regulating the cationic vacancy structure of NiO to optimize its d band center and accelerate oxygen evolution reaction. International Journal of Hydrogen Energy, 2024, 80: 907−915

[26] Ye C, Liu J, Zhang Q, et al. Activating metal oxides nanocatalysts for electrocatalytic water oxidation by quenching-induced near-surface metal atom functionality. Journal of the American Chemical Society, 2021, 143(35): 14169−14177

[27] Peng P, Hu X, Wang Q, et al. Quenching-induced interfacial amorphous layer containing atomic Ag on Fe_2O_3 nanosphere for high-performance lithium-ion batteries and mechanism. Journal of Colloid and Interface Science, 2022, 628: 736−744

[28] Zhang Y, He J, Yang Q, et al. Solution quenched *in-situ* growth of hierarchical flower-like $NiFe_2O_4/Fe_2O_3$ heterojunction for wide-range light absorption. Journal of Power Sources, 2019, 440: 227120

[29] Yang J, Wang Y, Yang J, et al. Quench-induced surface engineering boosts alkaline freshwater and seawater oxygen evolution reaction of porous $NiCo_2O_4$ nanowires. Small, 2022, 18(3): 2106187

[30] Chong L, Gao G, Wen J, et al. La- and Mn-doped cobalt spinel oxygen evolution catalyst for proton exchange membrane electrolysis. Science, 2023, 380(6645): 609−616

[31] Huang G, Hu M, Xu X, et al. Optimizing heterointerface of Co_2P–Co_xO_y nanoparticles within a porous carbon network for deciphering superior water splitting. Small Structures, 2023, 4(6): 2200235

[32] Chen K, Kim G C, Kim C, et al. Engineering core–shell hollow-sphere Fe_3O_4@FeP@nitrogen-doped-carbon as an advanced bi-functional electrocatalyst for highly-efficient water splitting. Journal of Colloid and Interface Science, 2024, 657: 684−694

[33] Dai F F, Xue Y X, Gao D L, et al. Facile fabrication of self-supporting porous $CuMoO_4$@Co_3O_4 nanosheets as a bifunctional electrocatalyst for efficient overall water splitting. Dalton Transactions, 2022, 51(33): 12736−12745

[34] Zhang L, Lin B W, Ye S Z, et al. Controllable disorder engineering in Mn-doped Co_3O_4/NF electrocatalyst for efficient overall water-splitting. Journal of Alloys and Compounds, 2023, 956: 170218

[35] Zhang Z, Liu X, Wang D, et al. Ruthenium composited $NiCo_2O_4$ spinel nanocones with oxygen vacancies as a high-efficient bifunctional catalyst for overall water splitting. Chemical Engineering Journal, 2022, 446: 137037

[36] Zhao X R, Yin F X, He X B, et al. Enhancing hydrogen evolution reaction activity on cobalt oxide in alkaline electrolyte by doping inactive rare-earth metal. Electrochimica Acta, 2020, 363: 137230

[37] Wu L, Zhou Z K, Xiao Y F, et al. Hydrogen evolution reaction activity and stability of sintered porous Ni–Cu–Ti–La_2O_3 cathodes in a wide pH range. International Journal of Hydrogen Energy, 2022, 47(21): 11101−11115

[38] Mo S, Zhang Q, Li S, et al. Integrated cobalt oxide based nanoarray catalysts with hierarchical architectures: *in situ* Raman spectroscopy investigation on the carbon monoxide reaction mechanism. ChemCatChem, 2018, 10(14): 3012−3026

[39] Zhong W, Yang C, Wu J, et al. Oxygen vacancies induced by charge compensation tailoring Ni-doped Co_3O_4 nanoflakes for efficient hydrogen evolution. Chemical Engineering Journal, 2022, 436: 134813

[40] Qu J, Ge Y, Zu B, et al. Transition-metal-doped p-type ZnO nanoparticle-based sensory array for instant discrimination of explosive vapors. Small, 2016, 12(10): 1369−1377

[41] Yang J, Zhang Z, Sun S, et al. Mo modified Co_3O_4 nanosheets array by a rapid quenching strategy for efficient oxygen evolution electrocatalysis. Frontiers in Materials, 2022, 9: 1089695